The Astrophysical Journal, 964:98 (18pp), 2024 March 20 https://doi.org/10.3847/1538-4357/ad20d3
© 2024. The Author(s). Published by the American Astronomical Society.
OPEN ACCESS

Recognizing Blazars Using Radio Morphology from the VLA Sky Survey

Zhang-Liang Xie (谢彰亮)[1], Eduardo Bañados[1], Silvia Belladitta[1,2], Chiara Mazzucchelli[3], Jan-Torge Schindler[4], Frederick Davies[1], and Bram P. Venemans[5]
[1] Max Planck Institut für Astronomie, Königstuhl 17, D-69117, Heidelberg, Germany
[2] INAF, Osservatorio di Astrofisica e Scienza dello Spazio, Via Gobetti 93/3, 40129 Bologna, Italy
[3] Instituto de Estudios Astrofísicos, Facultad de Ingeniería y Ciencias, Universidad Diego Portales, Avenida Ejercito Libertador 441, Santiago, Chile
[4] Hamburger Sternwarte, Universität Hamburg, Gojenbergsweg 112, D-21029 Hamburg, Germany
[5] Leiden Observatory, Leiden University, P.O. Box 9513, NL-2300 RA Leiden, The Netherlands
Received 2023 August 16; revised 2023 December 15; accepted 2023 December 18; published 2024 March 20

Abstract

Blazars are radio-loud active galactic nuclei whose jets have a very small angle to our line of sight. Observationally, the radio emissions are mostly compact or compact-core with a one-sided jet. With 2.″5 resolution at 3 GHz, the Very Large Array Sky Survey (VLASS) enables us to resolve the structure of some blazar candidates in the sky north of decl. −40°. We introduce an algorithm to classify radio sources as either blazar-like or non-blazar-like based on their morphology in the VLASS images. We apply our algorithm to three existing catalogs, including one of the known blazars (Roma-BzCAT) and two blazar candidates identified by Wide-field Infrared Survey Explorer colors and radio emission (WIBRaLS, KDEBLLACS). We show that in all three catalogs, there are objects with morphologies inconsistent with being blazars. Considering all the catalogs, more than 12% of the candidates are unlikely to be blazars, based on this analysis. Notably, we show that 3% of the Roma-BzCAT *confirmed* blazars could be a misclassification based on their VLASS morphology. The resulting table with all sources and their radio morphological classification is available online.

Unified Astronomy Thesaurus concepts: Blazars (164); Active galactic nuclei (16); Radio jets (1347)

Supporting material: machine-readable tables

1. Introduction

Blazars are a subset of active galactic nuclei (AGN) that have radio jets pointed toward us at a very small angle ($\theta < 20°$, Kollgaard et al. 1992; Urry & Padovani 1995). Despite being one of the rarest subclasses of AGN, they are the most commonly found sources in the γ-ray sky (e.g., Hartman et al. 1999; Ajello et al. 2020). Blazars are highly variable and polarized radio sources that exhibit compact morphology. Additionally, they are luminous across a wide range of frequencies, spanning from the radio to γ-ray (Blandford & Königl 1979; Abdo et al. 2010). Observational signs of jets can be found across a broad range of the electromagnetic spectrum (Blandford et al. 2019). In particular, blazars can be classified into two subclasses based on their optical/near-infrared emission lines: BL Lacertae objects (BL Lac), which have either no or very weak emission lines (with a rest-frame equivalent width of <5 Å; Stickel et al. 1991), and flat spectrum radio quasars (FSRQ), which have broad optical/near-infrared emission lines similar to those of Type 1 quasars and a flat radio spectrum (Sambruna et al. 1996).

A large sample of blazars is necessary to study their radiation mechanism and relativistic jet-beaming effects. However, confirming a large number of blazars is time- and resource-consuming (e.g., Shaw et al. 2012). Roma-BzCAT is currently the most comprehensive collection of confirmed blazars, containing 3561 sources that are classified as BL Lac or FSRQ (Massaro et al. 2015). All blazars in Roma-BzCAT must meet the criteria of having spectroscopic information showing characteristic features of their class, at least one radio detection exhibiting compact morphology or a one-sided jet, and an isotropic X-ray luminosity close to or higher than 10^{43} erg s^{-1} (Massaro et al. 2009).

In an effort to expand the pool of identified blazars while minimizing the presence of potential contaminants, primarily other forms of AGN, D'Abrusco et al. (2012) studied the mid-infrared (MIR) colors of established blazars, employing the Wide-field Infrared Survey Explorer (WISE; Wright et al. 2010) to uncover a distinctive color region in which blazars reside. D'Abrusco et al. (2014) assembled a catalog of blazar candidates (WIBRaLS) based on their WISE IR colors (W1−W2, W2−W3, W3−W4), while requiring the existence of a radio counterpart either in the NRAO VLA Sky Survey (NVSS; Condon et al. 1998) or the Sydney University Molonglo Sky Survey (SUMSS; Mauch et al. 2008). More recently, they used a larger sample of confirmed blazars and radio data from the Faint Images of the Radio Sky at Twenty-cm survey (FIRST; Becker et al. 1994) to recognize additional blazar candidates (WIBRaLS2; D'Abrusco et al. 2019). They also established a second catalog, KDEBLLACS, which employs only W1–W2 and W2–W3 colors (i.e., excluding a W4 requirement) to detect fainter candidates. KDEBLLACS sources also must have a radio counterpart. The total number of blazar candidates from WIBRaLS, WIBRaLS2, and KDEBLLACS is 17,996. A recent study by de Menezes et al. (2019) analyzed the Sloan Digital Sky Survey spectra for available objects in the D'Abrusco et al. (2019) catalogs and estimated that $\gtrsim$40% of them are contaminants, primarily quasars and galaxies. While spectroscopic follow-up is essential for determining the nature of blazar candidates, an approach for removing contaminants from a large pool of blazar candidates would greatly aid in more efficient follow-up investigations to

Original content from this work may be used under the terms of the Creative Commons Attribution 4.0 licence. Any further distribution of this work must maintain attribution to the author(s) and the title of the work, journal citation and DOI.

determine their true nature. We notice that at the angular resolution of radio surveys used by D'Abrusco et al. (2014, 2019) (∼45″ for both NVSS and SUMSS, ∼5″ for FIRST), the radio structure for most blazar candidates is not resolved, particularly for sources outside the FIRST footprint.

In this work, we take advantage of the radio images of the Very Large Array Sky Survey (VLASS; Lacy et al. 2020; Gordon et al. 2021). At the time of this study, VLASS provides two epoch[6] 3 GHz images for all the sky above decl. $> -40°$ at a higher angular resolution than previous large sky radio surveys (∼2.″5). Since the blazar's jet is directed toward us at a small angle, the VLASS radio morphology is expected to be compact. We note that the actual morphology of blazars could be more complicated. For example, Kharb et al. (2010) showed that some of the blazars in the MOJAVE (Monitoring Of Jets in Active galactic nuclei with Very Long Baseline Array (VLBA) Experiments; Lister et al. 2021) sample exhibit both compact and extended emission at 1.4 GHz. However, we will show that at the VLASS frequency, resolution, and sensitivity, most of the MOJAVE blazars are classified as compact objects. Thus, if the VLASS images resolve a clear two-sided jet pattern, we can conclude that the radio source is likely not a blazar.

The focus of this paper is the introduction of an automated algorithm that utilizes publicly available VLASS 3 GHz radio images to classify sources whose morphologies are compatible or not with being blazars. This paper is structured as follows: In Section 2, we present an overview of the data used in this study. Section 3 describes our algorithm for automatically classifying VLASS sources based on their morphology. We present the automated classification of all sources in Section 4. In Section 5, we discuss sources with mismatched positions in the blazar catalog. We also discuss the appearance of MOJAVE blazars and their classification with VLASS 3 GHz images. We summarize our work in Section 6. Throughout this study, we adopt a flat ΛCDM cosmology with $H_0 = 70\,\mathrm{km\,s^{-1}\,Mpc^{-1}}$, $\Omega_M = 0.3$, and $\Omega_\Lambda = 0.7$, and all magnitudes are reported in the AB magnitude system.

2. Data

Our data set comprises a combination of three catalogs: Roma-BzCAT (Massaro et al. 2015), WIBRaLS (D'Abrusco et al. 2014, 2019), and KDEBLLACS (D'Abrusco et al. 2019). WIBRaLS and KDEBLLACS contain blazar candidates, while Roma-BzCAT consists of confirmed blazars. We download all available epochs of the VLASS Quick Look Images for the sources in this data set. VLASS1.1 corresponds to the first epoch of the first half of the sky, and VLASS1.2 is the first epoch of the second part of the sky. The first epoch is completed in 2019, while the second epoch, VLASS2.1 and VLASS2.2, is completed in June 2022. There are upgrades in the image processing pipeline between epochs 1 and 2, producing cleaner radio images for both faint and bright sources by fixed pipeline issues (for more details, refer to Lacy et al. 2022).

The blazar candidates in WIBRaLS/WIBRaLS2 (hereafter referred to as WIBRaLS) are selected based on two criteria that must be satisfied simultaneously: (i) having similar WISE colors (W1−W2 and W2−W3, and W3−W4) as known blazars in Roma-BzCat, and (ii) having a radio counterpart. Meanwhile, KDEBLLACS complements WIBRaLS by adding fainter candidates not detected in the W4 band.

Initially, our data set includes a total of 12,416 blazar candidates from the WIBRaLS and WIBRaLS2 catalogs. We find that 9821 candidates have VLASS Quick Look Image coverage, with 9061 sources having two VLASS epochs and 220 sources having only one epoch. For KDEBLLACS, there are a total of 4996 out of 5580 sources with VLASS coverage, with 4926 two-epoch sources and 70 one-epoch sources. Out of 3561 blazars in Roma-BzCAT, 3134 sources have VLASS images, with 3078 sources having two-epoch images and 56 sources having only one epoch. We do not differentiate between subclasses of blazars in this study.

3. Method

3.1. Automated Algorithm of Morphology Recognition

In VLASS images, jet patterns are easily recognizable by the human eye, and manual morphological classification can be achieved through visual inspection. However, our objective is to develop an automated algorithm that can mimic human visual classification in an objective and reproducible way. To achieve this, we download 2′ × 2′ VLASS images centered on known blazar/candidates with catalog coordinates, and utilize the `zscale` algorithm (Tody 1986) to process the images into machine-readable masked values. The `zscale` algorithm is specifically designed to display images near their median in a computationally efficient way without the need to compute the entire pixel value distribution histogram. This algorithm is particularly useful in highlighting peaked patterns that are brighter than the background, making them more discernible in astronomical images. The `zscale` algorithm returns two limits in pixel values denoted as $zs_{\rm up}$ and $zs_{\rm low}$. Pixels whose values are above $zs_{\rm up}$ appear bright, while those with values below $zs_{\rm low}$ appear dark.

Next, our algorithm focuses specifically on pixels with values $\geqslant zs_{\rm up}$, as these pixels provide a good representation of the source's morphology of their radio emission. By only calculating the distribution of the brightest pixels, the algorithm can obtain a proxy of the source's morphology, as shown by the black contours in Figure 1.

The next goal is to classify the morphology, estimated by the highlighted pixel in each image. Our algorithm transforms the shape of the source in the VLASS image onto two 1D lines, generated by stacking the pixel counts in the respective direction. The height and width of the single-/multi-peaked 1D curve in the resulting plots represent the morphological characteristics of the radio source (see Figure 1 for an example).

3.2. Classifications on Morphologies

Our algorithm provides a morphological classification for each image by analyzing the shape of the signals obtained from processing the VLASS images into 1D curves. The algorithm classification can then be split into two groups: those displaying blazar-like and non-blazar-like morphologies. Examples of all subclasses are shown in Figure 2. Below, we explain how we identify each morphology classification from their 1D signal.

We categorize all sources with blazar-like morphologies into four subclasses: COMPACT, OFFSET, 1-SIDE SEPARATED,

[6] In 2023 January, VLASS started observing a third epoch of the sky. We only use the first two epochs in this study.

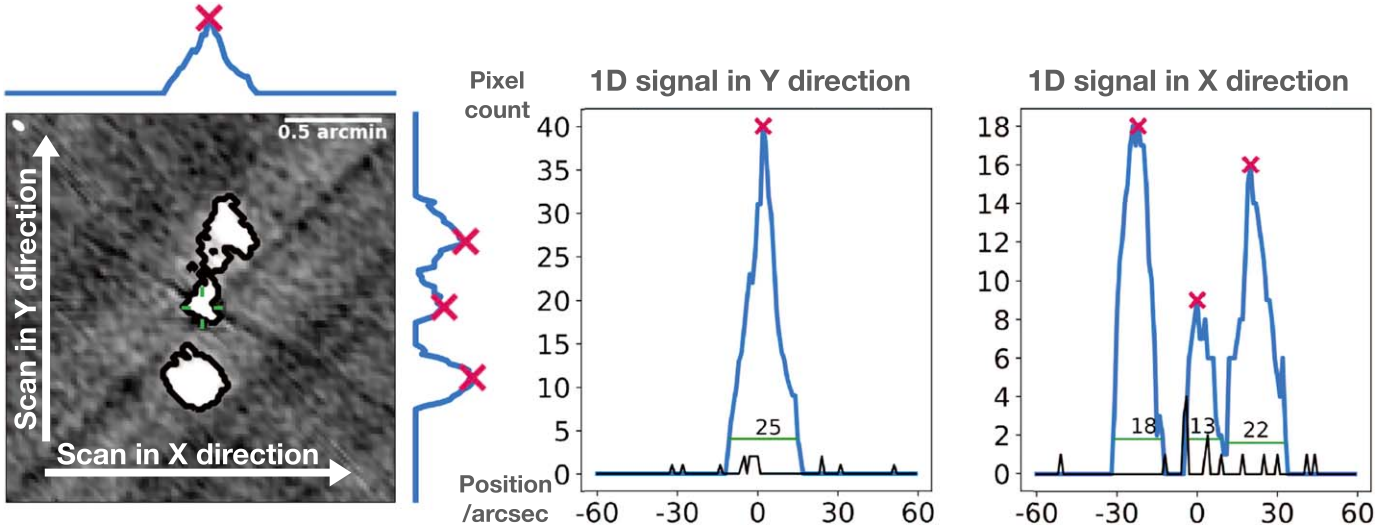

Figure 1. An illustration of the automated morphological classification algorithm applied to VLASS images (The beam size is denoted in the top left corner and is approximately $1\farcs8 \times 2\farcs9$). The algorithm processes each image, converting it into binary values (marked sections are depicted by black contour lines) based on their flux. Each of the 1D curves (blue line) represents the pixel count in a single scanning row in the selected direction, denoted by the white arrows in the image. Cross markers overlaid on the 1D curve indicate peak locations within the 1D curve, which are used to assign morphological classifications to the sources. A green line on the plot represents the peak width measured by each of their relative heights. The value in the number of pixels is shown, which also contributes to determining the morphological class of the sources (refer to Section 3.2 for details).

and 1-SIDE EXTENDED. We list the details for each blazar-compatible subclass and their morphological features below:

COMPACT: The VLASS image exhibits a compact unresolved source, indicating that the morphology is consistent with a jet directed toward us at a very small angle (see Figure 2, top left). A COMPACT source is identified as a single peak in both row and column 1D signal, representing a single bright pixel cluster located in the central region of the VLASS image.

OFFSET: The radio image shows one source that resembles the COMPACT class, but whose optical/MIR coordinates are offset from the compact radio source. To determine a source as OFFSET, we examine the positions of two peaks in a row and column signals and calculate the offset value by measuring the distance to the catalog position. We classify sources as OFFSET when their compact radio emission is at least $5''$ away from the position listed in the catalogs (see Figure 2, bottom left as an example). This can happen when using lower-resolution radio surveys than VLASS and incorrectly associating the radio emission from another close source with its optical counterpart. A source is not classified as OFFSET if its offset surpasses $10''$, to avoid potential misidentification with an incorrect source deviating from the catalog position. For additional details, refer to Section 5.1.

1-SIDE SEPARATED: The radio image reveals two distinct radio sources, with one precisely at the location of a confirmed blazar or blazar candidate. Such a morphology is recognized as a typical blazar morphology in Roma-BzCAT (Figure 2, top middle). For a 1-SIDE SEPARATED source, the 1D signal displays exactly two peaks, either in a row or column, or both, depending on the jet's orientation. If the jet aligns with the row or column direction, only a single peak will be observed in the corresponding direction.

1-SIDE EXTENDED: The radio image exhibits a connected, extended structure with its core aligning with the catalog position of the blazar or blazar candidate. In this scenario, the jet extends to one side. Similar to the 1-SIDE SEPARATED morphology, this configuration also represents a central source emitting a jet oriented toward us at a small angle, and it is thus considered to be compatible with a blazar morphology (Figure 2, bottom middle). The 1D signal displays a single peak in both row and column, as the center is connected with the extended radio lobe, suggesting only one radio blob exists in the image. However, the peak should also have a width larger than $15''$. We choose this value to be greater than a circle centering at the source, where we estimate the dynamic range to identify potential artifacts. This area has a radius of $7''$ ($\sim$2–3 times the beam size, see also Section 3.3 for details). Consequently, the peak position is not centrally located but shifted in the projected direction that the jet extends.

We identify sources that show two-side symmetrical jets as likely non-blazars, implying their viewing angle is likely not close to our line of sight. The two subclasses of sources with non-blazar-like morphologies are described below (also refer to the right side of Figure 2):

2-SIDE SEPARATED: The radio image displays two symmetrical jets on either side of the central core. The observed comparable separations for both jets in 2-SIDE SEPARATED sources suggest that the jets are nearly perpendicular to our line of sight, thereby excluding them as blazars. The 1D signal exhibits exactly three peaks in a row and/or column. Similar to the 1-SIDE SEPARATED morphology, the jet angle can influence the number of detected peaks. If the jets align with either row or column, fewer than three peaks will be displayed. However, the other direction will still identify three peaks, classifying the source as a 2-SIDE SEPARATED morphology.

2-SIDE EXTENDED: The radio image presents two symmetrical jets, similar to the *2*-SIDE SEPARATED objects. The distinguishing feature of 2-SIDE EXTENDED sources

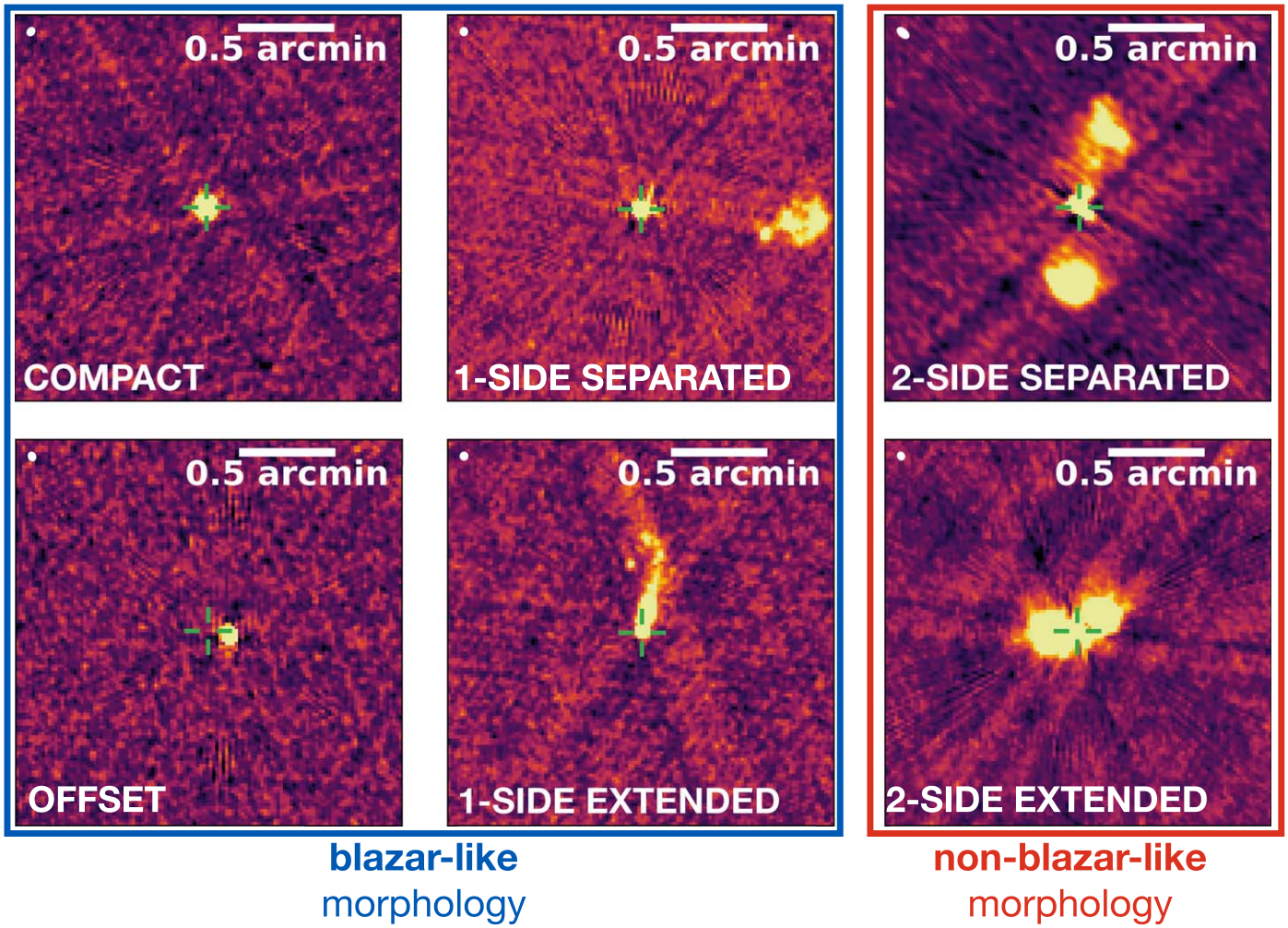

Figure 2. Morphological classification of VLASS images using our automated algorithm. The images are categorized into six distinct morphological classes, grouped into two sets. Blazar-like morphologies include COMPACT, OFFSET, 1-SIDE EXTENDED, and 1-SIDE SEPARATED, while non-blazar-like morphologies comprise 2-SIDE EXTENDED and 2-SIDE SEPARATED. In each morphological class, their corresponding 1D signals are shown in two directions, indicated by blue lines. Automatically identified peaks are marked by pink crosses, with morphological classification determined by the properties of peaks, including number, width, and distance to the center position. Descriptions of each morphological class and their characteristics can be found in Section 3.2.

is that the lobes and the core are interconnected at the resolution of our images, exhibiting similar extension sizes. Following the same logic as the 2-SIDE SEPARATED case, these jets must be nearly perpendicular to our line of sight. In the 1D signal of a 2-SIDE EXTENDED source, the peak is closer to the center than in 1-SIDE EXTENDED, as the jets extend from the central source in both directions rather than just one. We determine that if the peak (center of the radio source) is within 10″ (∼3 times the beam size, also being out of the 7″ circle where we assess the dynamical range) from the catalog position, it will be categorized as 2-SIDE EXTENDED; otherwise, it will be regarded as 1-SIDE EXTENDED.

In addition to blazar-like and non-blazar-like classifications, we observe sources that exhibit no visible radio emission in VLASS images. We categorize these sources as NON-DETECTION.

NON-DETECTION: The radio image displays no visible features near the catalog position. We assess the signal-to-noise ratio (S/N) to determine if the source is detected. The S/N is computed as the peak flux density within a 10″ circle surrounding the source, divided by the noise. The noise for each image is the rms value of all pixels, following a 2.5σ clipping of the image. If a source's S/N is below 5.0, it will be classified as a NON-DETECTION. The 1D signal reveals no significant peaks exceeding the noise level (for example, see the right panel in Figure 3).

This classification approach effectively distinguishes morphologies within a vast amount of radio data. The conversion from 2D images to 1D curves is both straightforward and rapid. The algorithm reduces the data processing complexity from $O(n^2)$ (pixels in two dimensions) to $O(n)$ (pixels in one dimension). Additionally, our classification method requires no prior models, calibrators, or training sets.

3.3. Quality Check

The majority of sources in all data sets are present in both VLASS epochs (VLASS1.1/1.2 and VLASS2.1/2.2, refer to Section 2). We independently apply the algorithm to these two epochs. We first assign quality flags to the image in each of the epochs. If both epochs result in the same morphological

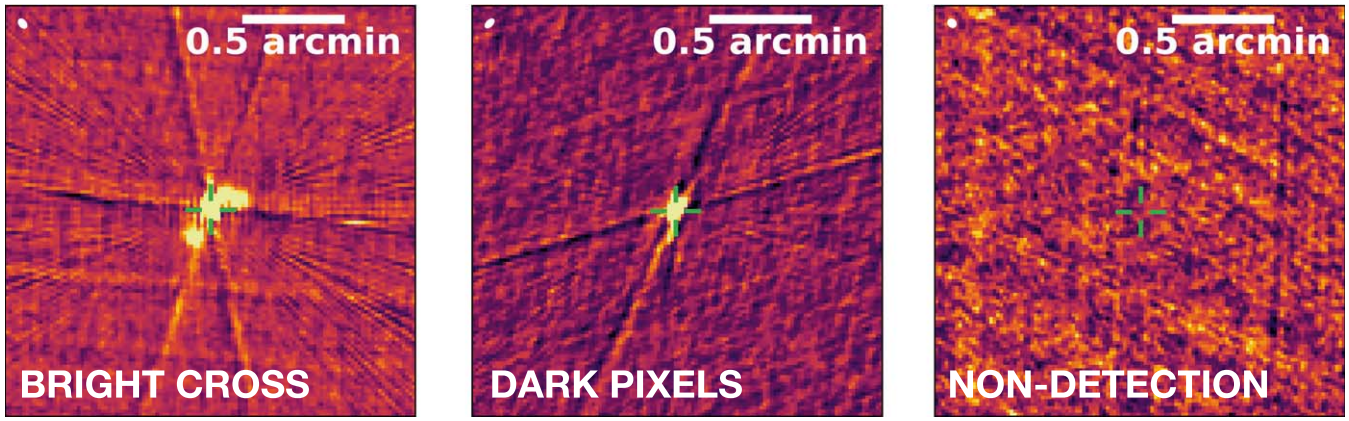

Figure 3. An illustration of two artifact types and a NON-DETECTION source in VLASS images. The algorithm identifies cross pattern and dark pixel artifacts, assigning appropriate quality flag values (1 for cross pattern presence, 2 for dark pixel presence, and 3 for both artifacts in the image). Sources with low S/Ns that are difficult to discern by visual inspection are classified as NON-DETECTION sources.

classification, it is considered final. However, in cases of discrepancy, the final classification will be determined by the image of superior quality. The process is as follows:

1. We first define a quality flag with a value ranging from 0 (best quality) to 3 (worst quality). Further details are provided below. If one of the epochs has a superior quality flag compared to the other, the morphology from that epoch is considered the final classification. If the quality flags are identical, but the classifications from each epoch remain inconsistent, we proceed to the next step.
2. The algorithm examines artifacts in the images, which may result from deficits in the clean algorithm and/or inadequate phase calibration during image production and that can affect the morphological classification (Lacy et al. 2022). We employ a quality flag to assess the impact of artifacts on the image. There are two types of artifacts we pay attention to, which we refer to as *bright crosses* and *dark pixels*:
   (a) Bright cross (Figure 3 left): This is a pattern of straight lines, composed of bright pixels (pixel value higher than $zs_{\rm up}$) traversing the image. It is identified by detecting narrow, low peak signals extending across the image. In the 1D signal, the algorithm counts the number of all peaks with pixel count (height of the 1D signal) less than 2. If the image displays more than 10 low peaks in the row and column directions combined, the quality flag is incremented by 1.
   (b) Dark pixels (Figure 3 middle): This pattern consists of dark pixels (pixel value lower than $zs_{\rm low}$) primarily located adjacent to the central bright source. The algorithm detects all pixels with values below $zs_{\rm low}$ in the 1D signal. After visually inspecting several instances of this artifact, we establish that if the sum of all dark pixels exceeds 30% of the sum of all bright pixels, the quality flag is incremented by 2.

If one epoch has a lower-quality flag value, the morphology of that epoch is considered final. In cases where both images have the same quality flag, thus similarly affected by artifacts, we proceed to the following step.

1. The algorithm calculates the ratio of the total sum of dark pixels to the total sum of bright pixels. The epoch with the smaller ratio prevails and is chosen as the final classification.

In addition to the aforementioned procedure, we implement an extra check for sources to be classified as COMPACT by assessing the dynamic range value. This is because artifacts can mislead the algorithm into incorrectly interpreting them as sidelobes. The dynamic range is a metric to discern the nature of a point source, mitigating the effects of artifact presence. To quantify the dynamic range, we employ the *peak-to-ring* metric from Gordon et al. (2021) and Lacy et al. (2022). We first calculate the peak flux value within a 2″ circle centered on the catalog position of the source, and then measure another peak flux within a 1″ wide annulus, where its inner boundary is 7″ away from the center (approximately two times the beam size for VLASS). We apply this measure to distinguish a core-dominated source when the images are affected by artifacts (when the epoch with the smallest quality flag value is greater than 0). In this case, if in any epoch the peak-to-ring ratio is larger than 2, the source will be classified as a COMPACT source. If none of the epochs (including the single-epoch sources) exceeds 2 in the peak-to-ring ratio, the source will be assigned as VISUAL NEEDED for further check. The final classification of these sources will be determined and assigned manually by us, following a visual check.

We assign a special category COMPACT_D to sources that comply with all the following: (i) a peak-to-ring dynamic range greater than 2, (ii) the smallest quality flag between both epochs exceeds 1, and (iii) the source was classified as NON-COMPACT in both VLASS epochs. This implies that the artifacts probably cause the seemingly extended feature. For the sources with only one epoch image available, the source will first be checked if it is detected. It will be classified as a NON-DETECTION if its S/N value is below 5. The automated classification is final when the quality flag is not larger than one. If the quality flag of the image exceeds 1, and the peak-to-ring dynamic range is greater than 2, the source will be assigned as COMPACT_D. Otherwise, the source will be classified as VISUAL NEEDED to be visually classified.

4. Result of the Algorithm Classification

We apply our morphological classification algorithm to a total of 9821 VLASS sources from the WIBRaLS catalog, 4996 sources from the KDEBLLACS catalog, and 3134

Table 1
Sources from the Roma-BzCAT Catalog Processed and Classified Using Our Algorithm

No.[a]	Name[b]	R.A.[c]	Decl.[d]	Class[e]	VFlag[f]	VClass[g]	SEpoch[h]
1	J000020.39-322101.00	0.08495833333	−32.35027778	COMPACT_D	0	…	…
2	J000105.29-155106.98	0.2720416667	−15.85193889	COMPACT	0	…	…
3	J000108.62+191434.18	0.2859166667	19.24282778	COMPACT	0	…	
156	J010838.76+013500.31	17.1615	1.583419444	COMPACT	0	…	EP02
1185	J100021.79+223318.61	150.0907917	22.55516944	2-SIDE EXTENDED	1	…	…
2566	J174805.82+340401.20	267.02425	34.067	2-SIDE EXTENDED	1	COMPACT	…
2677	J193109.60+093717.50	292.7882083[i]	9.6211944[i]	OFFSET	1	…	…
2805	J211720.72+050257.58	319.3363333	5.049327778	VISUAL NEEDED	1	COMPACT	…
3132	J235846.08+195520.31	359.692	19.92230833	COMPACT_D	0	…	…
3133	J235859.86+392228.30	359.7494167	39.37452778	COMPACT_D	0	…	…
3134	J235933.18+385042.28	359.88825	38.84507778	COMPACT	0	…	…

Notes. Each source is analyzed based on available radio images from two VLASS epochs, with the algorithm assigning a final morphological classification. Each visually inspected source has a "VFlag" of 1. If the visual classification ("VClass") does not match the algorithm classification ("Class"), we update VClass to the correct classification. For sources labeled with VISUAL NEEDED, their class is determined visually and assigned to VClass. We look into all non-blazar-like sources according to the algorithm in Roma-BzCAT to verify their morphology; more details are in the Appendix. The full table is available online.
[a] Number in the result catalog.
[b] Name of the source.
[c] R.A. (J2000).
[d] decl. (J2000).
[e] Morphological classification decided by the algorithm;
[f] Visual flag, 1 if the source is visually inspected, 0 if not.
[g] Visual classification, assigned by human eyes if the algorithm classification is wrong, this entry is left empty if the source is not visually inspected or the algorithm classification is correct when "VFlag" is 1.
[h] If the source has two epochs available, this column is left empty, otherwise, it will denote which epoch of VLASS images is available for the source, EP01: VLASS1, EP02: VLASS2.
[i] Corrected value by crossmatching with MilliQuas catalog, more details refer to Section 5.1.

(This table is available in its entirety in machine-readable form.)

Table 2
Same as Table 1 for WIBRaLS

No.	Name	R.A.	Decl.	Class	VFlag	VClass	SEpoch
1	J000020.40-322101.24	0.085	−32.35034444	COMPACT_D	0	…	…
2	J000029.08-163620.24	0.1211666667	−16.60562222	COMPACT	0	…	…
3	J000047.05+312028.21	0.1960416667	31.34116944	COMPACT	0	…	…
4	J000101.05+240842.52	0.254375	24.14514444	COMPACT	0	…	…
5	J000105.29-155107.21	0.2720416667	−15.85200278	COMPACT	0	…	…
9817	J235919.53-204756.10	359.831375	−20.79891667	2-SIDE EXTENDED	0	…	…
9818	J235931.80-063943.37	359.8825	−6.662047222	COMPACT	0	…	…
9819	J235935.23+522236.85	359.8967917	52.37690278	COMPACT	0	…	…
9820	J235941.29+392439.47	359.9220417	39.41096389	COMPACT	0	…	…
9821	J235951.04+470709.41	359.9626667	47.11928056	COMPACT	0	…	…

(This table is available in its entirety in machine-readable form.)

sources from the confirmed blazars in the Roma-BzCAT catalog. A portion of the results for the Roma-BzCAT catalog is presented in Table 1. This table includes the name generated by the algorithm in the form of hh:mm:ss.ss ± dd:mm:ss.ss, coordinates, and the assigned morphological classification. Blazar-like morphologies consist of COMPACT, 1-SIDE SEPARATED, and 1-SIDE EXTENDED categories. Non-blazar-like morphologies are 2-SIDE SEPARATED and 2-SIDE EXTENDED.

In Roma-BzCAT, we conduct a visual inspection of all non-blazar-like sources. In cases where the visual classification differs from the algorithm-based classification, we assign the accurate classification to VClass. We discuss and show VLASS2 images of all non-blazar-like sources in the Appendix. The tables with the same entries have also been generated for the WIBRaLS and KDEBLLACS catalogs (refer to Table 2 for WIBRaLS and Table 3 for KDEBLLACS). We do not visually check all non-blazar-like sources in these two catalogs.

Table 4 provides a summary of our morphological classification of all sources from the Roma-BzCAT, WIBRaLS, and KDEBLLACS catalogs with corresponding VLASS images. Approximately 95% of sources in the Roma-BzCAT catalog exhibit morphologies consistent with blazars, while 86% of sources in the WIBRaLS catalog and 88% of sources in the KDEBLLACS catalog are similarly consistent with being blazars.

The lower *contamination* rate (i.e., sources unlikely to be blazars) within the Roma-BzCAT catalog is expected, as this curated catalog requires each source to have spectroscopic

Table 3
Same as Table 1 for KDEBLLACS

No.	Name	R.A.	Decl.	Class	VFlag	VClass	SEpoch
1	J000007.63+420725.51	0.03179166667	42.12375278	NON-DETECTION	0	…	…
2	J000010.29-363405.26	0.042875	−36.56812778	COMPACT	0	…	…
3	J000056.23-082742.05	0.2342916667	−8.461680556	COMPACT	0	…	…
4	J000116.38+293534.59	0.31825	29.59294167	COMPACT	0	…	…
5	J000126.44+733042.60	0.3601666667	73.51183333	COMPACT	0	…	…
4992	J235859.76+431617.64	359.749	43.27156667	COMPACT	0	…	…
4993	J235901.15+171925.84	359.7547917	17.32384444	COMPACT	0	…	…
4994	J235932.16-121022.56	359.884	−12.17293333	COMPACT	0	…	…
4995	J235944.89+054431.34	359.9370417	5.742038889	COMPACT	0	…	…
4996	J235955.31+314559.85	359.9804583	31.766625	COMPACT	0	…	…

(This table is available in its entirety in machine-readable form.)

Table 4
Statistics of Different VLASS Morphological Classifications for All Sources in Roma-BzCAT, WIBRaLS, and KDEBLLACS

		Blazar-like Morphology				Non-blazar-like Morphology		
Catalog	TOTAL	COMPACT/_D	COMPACT OFFSET	1-SIDE SEP	1-SIDE EXT	2-SIDE SEP	2-SIDE EXT	NON-DET
Roma-BzCAT	3134	2835/1144 (90.5%)	6 (<1%)	112 (3.6%)	20 (<1%)	36* (1.1%)	105* (3.4%)	13 (<1%)
WIBRaLS	9821	7326/1491 (74.6%)	72 (<1%)	958 (9.8%)	64 (<1%)	703 (7.2%)	506 (5.2%)	90 (<1%)
KDEBLLACS	4996	4103/67 (82.1%)	233 (4.7%)	76 (1.5%)	6 (<1%)	36 (<1%)	3 (<1%)	356 (7.1%)

Note. We identify four classes as compatible with blazar-like morphologies and two classes as non-blazar-like morphology. The sources that are classified as COMPACT_D are included in COMPACT sources (see details in Section 3.3) and the separate number of this class is listed. The percentage of non-blazars in WIBRaLS (12%) is higher than in Roma-BzCAT (4%), which is expected given that WIBRaLS consists of candidates, while Roma-BzCAT is a curated catalog. In a test sample of 1000 sources from Roma-BzCAT, the classification accuracy is 90.6%.
[a] We conduct a visual examination of every non-blazar-like source in Roma-BzCat. The number reported here is the result after visual inspection, ruling out all false classifications. For more details, refer to the Appendix.

information to establish its blazar type (BL Lac or FSRQ). However, it is noteworthy that 4.5% of sources (141) are classified as non-blazar-like sources. We visually inspect each source and find that 106 sources indeed show morphologies that are likely not blazars. A closer examination of the multiwavelength properties of these 106 Roma-BzCAT sources is required to ascertain their actual nature. All sources are shown in the Appendix.

To evaluate the algorithm's accuracy, we randomly select 1000 sources from the Roma-BzCAT catalogs. We conduct a visual inspection of these 1000 sources and assign a visual morphology classification, following the same naming convention used by our algorithm. By considering the visual inspection classification as the ground truth, the accuracy of the classifier is at the percent of 90.6% for the 1000 source sample. The classifier makes mistakes by confusing artifacts with actual features in the morphology. These artifacts, as shown in Figure 3, have signals that resemble the real radio signals emitted by the source.

5. Discussion

5.1. Misidentifications of OFFSET Sources

OFFSET sources are present in all three catalogs of our data set. This class of sources is characterized by the absence of radio emission at the catalog position. Instead, radio emission is observed with an offset (5″–10″) from the position registered in the catalog. For OFFSET sources in Roma-BzCAT, it is important to note that the spectroscopic information for the central source has already been obtained, allowing for the determination of a specific blazar type (Massaro et al. 2009).

For the six OFFSET sources in the Roma-BzCAT catalog, we examine their available archival data. Four of the six sources show real offset (shown in Figure 4); the other two sources show no actual offset in their VLASS images and the optical counterpart is at the exact position of the radio source. Thus, they are classified as COMPACT sources instead. We perform crossmatching to the MilliQuas catalog (Flesch 2021) within a range of 5″–10″ and discover that all four sources were mispositioned in the Roma-BzCAT catalog; instead, all four sources have previous information on the precise position of their counterparts in X-ray or other wavelengths. The positions reported in the literature align with the actual VLASS radio source and there is no offset in their optical counterpart as well. Here, we provide information on the optical counterparts information for the four OFFSET sources:

J193109.60+093717.50: The optical position is provided in Motch et al. (1998). They carried out the observation at Observatoire de Haute-Provence, CNRS, France, to acquire the optical position and also identify a featureless spectrum to confirm its BL Lac nature.

J205243.03+081037.48: It is included in a spectroscopic campaign done by Piranomonte et al. (2007). They observe this source with the 3.6 m Telescopio Nazionale Galileo. The optical position is determined and its spectrum also shows the absence of emission or absorption features, a BL Lac characteristic.

J230635.50-110349.28 and J232352.50+421054.98: Their positions are recorded in Bauer et al. (2000). They carry out

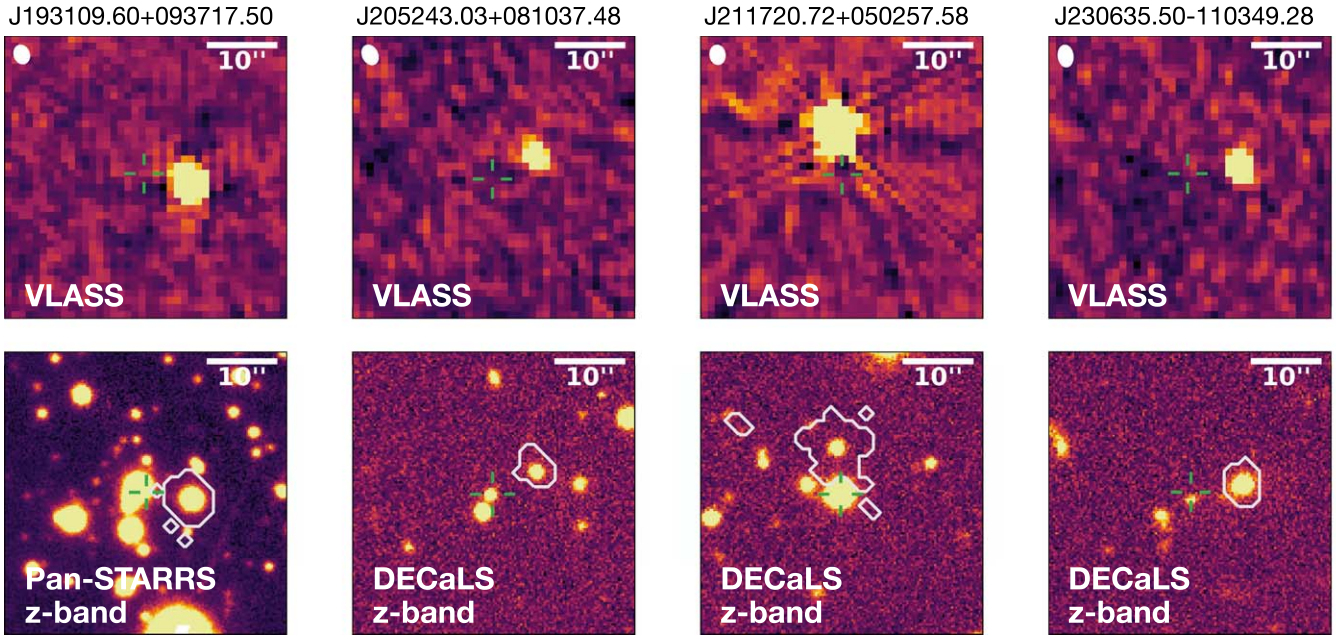

Figure 4. OFFSET sources from Roma-BzCAT, four in total. These sources are classified based on the discrepancy between the catalog position and the position of the radio source. The green cross represents the source position recorded in Roma-BzCAT. The radio image (upper row) demonstrates that the radio-emitting source is not located at the catalog position but has an offset of more than 5″. In the optical *z*-band image (lower row), a separate radio-silent source is found at the catalog position. This mismatch is a position error in Roma-BzCAT and we provide the accurate coordinates in our result.

Table 5
Same as Table 1 for MOJAVE Sources

No.	Name	R.A.	Decl.	Class	VFlag	VClass	SEpoch
1	S4 0003+38	1.48823	38.33754	COMPACT	0	…	…
2	NRAO 005	1.55789	−6.39315	COMPACT	0	…	…
3	CRATES J0009+0628	2.26638	6.47257	COMPACT	0	…	…
4	III Zw 2	2.62919	10.97486	COMPACT	0	…	…
5	4C +40.01	3.37971	40.86032	2-SIDE EXTENDED	1	…	…
405	1ES 2344+514	356.77015	51.70497	COMPACT	0	…	…
406	PKS 2345-16	357.01087	−16.52001	COMPACT_D	0	…	…
407	4C +45.51	358.59033	45.88451	COMPACT	0	…	…
408	S5 2353+81	359.09497	81.88118	COMPACT	0	…	…
409	PKS 2356+196	359.69202	19.92231	COMPACT	0	…	…

(This table is available in its entirety in machine-readable form.)

cross-identifications to match NVSS sources to bright X-ray sources and provide the coordinates of the closest matches. J232352.50+421054.98 was classified as a BL Lac object based on its archival spectrum.

We inspect all coordinates above and confirm that they are located on the center of radio sources in VLASS images. We have updated the positions of these mispositioned sources in the Roma-BzCAT catalog and included them in our output catalog for accurate reference (see Table 1 for an example).

5.2. Testing the Algorithm on the MOJAVE Blazars

The MOJAVE survey focuses on obtaining high-resolution images of AGN radio jets using VLBA observations, providing detailed images at the parsec level. We ran our VLASS classifier algorithm in 320 MOJAVE sources that are identified as blazars (Lister et al. 2021). The result is that 298 are classified as having blazar-like morphology. The VLASS images of the 22 non-blazar-like sources (2-SIDE EXTENDED or 2-SIDE SEPARATED)are shown in Figure 11. Out of those, 11 are still consistent with being compact sources, according to our visual inspection, resulting in 11 MOJAVE blazars with extended VLASS morphology. Our full classification for all 320 MOJAVE blazars is presented in an accompanying online table. A portion of the resulting table is presented in Table 5.

There are a few cases in which the MOJAVE blazars are known to display extended emission surrounding their compact core. For example, TXS 0716+714 (Antonucci et al. 1986; Wagner et al. 1996), PKS 1045-18, and PKS 1036+054 (see Figure 2 in Kharb et al. 2010). In these three examples, our algorithm classifies the sources as COMPACT_D. This means that some COMPACT_D sources might actually be extended (see Section 3.3), but still core dominated.

We find that 15 out of 320 MOJAVE sources are classified under COMPACT_D, including the examples above. However, without the knowledge of additional radio images of higher resolution or at different frequencies, we cannot differentiate if the extended morphology is real or introduced by artifacts.

In summary, MOJAVE blazars can display extended structures at both the submilliarcsecond scale in VLBA images and the kiloparsec scale in Very Large Array (VLA) 1.4 GHz

images. However, in most cases, these extended features are not discernible in the frequency and sensitivity of VLASS 3 GHz images due to low resolution or sensitivity. As a result, most sources are categorized as COMPACT objects, in line with their blazar characteristics (but see the Appendix for a discussion and images of MOJAVE sources classified as NON-COMPACT).

6. Summary

We develop an algorithm to classify radio sources into blazar-like or non-blazar-like based on their radio morphology on VLASS images. The algorithm classifies all sources into six morphological classes: four that are consistent with blazar morphologies and two non-blazar-like morphologies (see Figure 2 and Section 3). We apply the algorithm on three catalogs: WIBRaLS, which consists of blazar candidates with similar WISE color to known blazars; KDEBLLACS, which also includes blazar candidates selected by WISE color but undetected in the W4 band; and Roma-BzCAT, a catalog of known blazars based on a combination of spectroscopic identification, X-ray luminosity, and radio intensity and morphology in previous radio surveys. Our results indicate that all catalogs have sources that are unlikely to be blazars based on their morphology. In particular, WIBRaLS has a higher percentage of non-blazars (14%) compared to KDEBLLACS (12%), while Roma-BzCAT has the lowest percentage of seemingly non-blazars (5%, see Table 4) based on VLASS morphology. This is likely due to the low resolution of the radio surveys used by Roma-BzCAT, WIBRaLS, and KDEBLLACS to acquire radio counterparts and check morphology. Further details of our findings can be found in Section 4. We provide the morphological classifications in Tables 1–3. The full tables are available in the online journal.

We notice a specific population in all catalogs where the positions of some sources in the catalog do not match their radio source positions. We refer to these sources as OFFSET. Based on our analysis of four OFFSET sources in Roma-BzCAT, these discrepancies are due to positional errors. We provide the corrected position from crossmatching with other catalogs (see Section 5.1).

We also ran our algorithm on MOJAVE blazars, a collection of VLBA-monitored radio-active AGNs (Section 5.2). Although some MOJAVE blazars are known to show extended emission in VLBA and 1.4 GHz VLA images, 93% of MOJAVE blazars are classified as blazar-like sources by our algorithm using the VLASS 3 GHz images.

Our algorithm offers an efficient and rapid tool for identifying contaminants and cleaning blazar candidate catalogs. Further investigations involving spectroscopic and multi-wavelength follow-up can aid in pinpointing the true blazars and contaminants, and determining their properties. The future survey from SKA-Mid[7] (Dewdney et al. 2009) will have higher sensitivity and resolution than VLASS. This will allow us to examine the morphologies of radio sources, such as blazars, even in their earliest stages or at higher redshifts than currently possible.

The codes to reproduce this work and the resulting tables are available on Zenodo (European Organization For Nuclear Research & OpenAIRE 2013) under an open-source Creative Commons Attribution license: doi:10.5281/zenodo.10124636.

[7] https://www.skao.int/index.php/en/science-users/118/ska-telescope-specifications

Acknowledgments

We thank the referee for the critical assessment of the paper, pointing out the caveats of this work, which led to a substantial improvement of the manuscript.

The National Radio Astronomy Observatory is a facility of the National Science Foundation operated under cooperative agreement by Associated Universities, Inc.

This publication makes use of data products from WISE, which is a joint project of the University of California, Los Angeles, and the Jet Propulsion Laboratory/California Institute of Technology, funded by the National Aeronautics and Space Administration.

The Legacy Surveys consist of three individual and complementary projects: the Dark Energy Camera Legacy Survey (DECaLS; Proposal ID #2014B-0404; PIs: David Schlegel and Arjun Dey), the Beijing-Arizona Sky Survey (BASS; NOAO Prop. ID #2015A-0801; PIs: Zhou Xu and Xiaohui Fan), and the Mayall z-band Legacy Survey (MzLS; Prop. ID #2016A-0453; PI: Arjun Dey). DECaLS, BASS, and MzLS together include data obtained, respectively, at the Blanco telescope, Cerro Tololo Inter-American Observatory, NSF's NOIRLab; the Bok telescope, Steward Observatory, University of Arizona; and the Mayall telescope, Kitt Peak National Observatory, NOIRLab. Pipeline processing and analyses of the data were supported by NOIRLab and the Lawrence Berkeley National Laboratory (LBNL). The Legacy Surveys project is honored to be permitted to conduct astronomical research on Iolkam Du'ag (Kitt Peak), a mountain with particular significance to the Tohono O'odham Nation.

NOIRLab is operated by the Association of Universities for Research in Astronomy (AURA) under a cooperative agreement with the National Science Foundation. LBNL is managed by the Regents of the University of California under contract to the U.S. Department of Energy.

This project used data obtained with the Dark Energy Camera (DECam), which was constructed by the Dark Energy Survey (DES) collaboration. Funding for the DES Projects has been provided by the U.S. Department of Energy, the U.S. National Science Foundation, the Ministry of Science and Education of Spain, the Science and Technology Facilities Council of the United Kingdom, the Higher Education Funding Council for England, the National Center for Supercomputing Applications at the University of Illinois at Urbana-Champaign, the Kavli Institute of Cosmological Physics at the University of Chicago, Center for Cosmology and Astro-Particle Physics at the Ohio State University, the Mitchell Institute for Fundamental Physics and Astronomy at Texas A&M University, Financiadora de Estudos e Projetos, Fundacao Carlos Chagas Filho de Amparo, Financiadora de Estudos e Projetos, Fundacao Carlos Chagas Filho de Amparo a Pesquisa do Estado do Rio de Janeiro, Conselho Nacional de Desenvolvimento Cientifico e Tecnologico and the Ministerio da Ciencia, Tecnologia e Inovacao, the Deutsche Forschungsgemeinschaft and the Collaborating Institutions in the Dark Energy Survey. The Collaborating Institutions are Argonne National Laboratory, the University of California at Santa Cruz, the University of Cambridge, Centro de Investigaciones Energeticas, Medioambientales y Tecnologicas-Madrid, the University of Chicago, University College London, the DES-Brazil Consortium, the

University of Edinburgh, the Eidgenossische Technische Hochschule (ETH) Zurich, Fermi National Accelerator Laboratory, the University of Illinois at Urbana-Champaign, the Institut de Ciencies de l'Espai (IEEC/CSIC), the Institut de Fisica d'Altes Energies, Lawrence Berkeley National Laboratory, the Ludwig Maximilians Universitat Munchen and the associated Excellence Cluster Universe, the University of Michigan, NSF's NOIRLab, the University of Nottingham, the Ohio State University, the University of Pennsylvania, the University of Portsmouth, SLAC National Accelerator Laboratory, Stanford University, the University of Sussex, and Texas A&M University.

BASS is a key project of the Telescope Access Program (TAP), which has been funded by the National Astronomical Observatories of China, the Chinese Academy of Sciences (the Strategic Priority Research Program "The Emergence of Cosmological Structures" grant #XDB09000000), and the Special Fund for Astronomy from the Ministry of Finance. The BASS is also supported by the External Cooperation Program of the Chinese Academy of Sciences (grant #114A11KYSB20160057), and the Chinese National Natural Science Foundation (grant #12120101003, #11433005).

The Legacy Survey team makes use of data products from the Near-Earth Object Wide-field Infrared Survey Explorer (NEOWISE), which is a project of the Jet Propulsion Laboratory/California Institute of Technology. NEOWISE is funded by the National Aeronautics and Space Administration.

The Legacy Surveys imaging of the DESI footprint is supported by the Director, Office of Science, Office of High Energy Physics of the U.S. Department of Energy under Contract No. DE-AC02-05CH1123, by the National Energy Research Scientific Computing Center, a DOE Office of Science User Facility under the same contract; and by the U.S. National Science Foundation, Division of Astronomical Sciences under Contract No. AST-0950945 to NOAO.

The Pan-STARRS1 Surveys (PS1) and the PS1 public science archive have been made possible through contributions by the Institute for Astronomy, the University of Hawaii, the Pan-STARRS Project Office, the Max-Planck Society and its participating institutes, the Max Planck Institute for Astronomy, Heidelberg and the Max Planck Institute for Extraterrestrial Physics, Garching, The Johns Hopkins University, Durham University, the University of Edinburgh, the Queen's University Belfast, the Harvard-Smithsonian Center for Astrophysics, the Las Cumbres Observatory Global Telescope Network Incorporated, the National Central University of Taiwan, the Space Telescope Science Institute, the National Aeronautics and Space Administration under Grant No. NNX08AR22G issued through the Planetary Science Division of the NASA Science Mission Directorate, the National Science Foundation Grant No. AST-1238877, the University of Maryland, Eotvos Lorand University (ELTE), the Los Alamos National Laboratory, and the Gordon and Betty Moore Foundation.

This research has made use of data from the MOJAVE database that is maintained by the MOJAVE team (Lister et al. 2018). This research has made use of the SIMBAD database, operated at CDS, Strasbourg, France (Wenger et al. 2000).

Sofware. We use the following software and packages throughout the work: `APLpy` (Robitaille & Bressert 2012), `AstroPy` (Astropy Collaboration et al. 2013, 2018, 2022), `Astroquery` (Ginsburg et al. 2019), `Matplotlib` (Hunter 2007), `NumPy` (van der Walt et al. 2011; Harris et al. 2020), `Pandas` (McKinney 2010; Reback et al. 2022), `SAOImage DS9` (Joye & Mandel 2003), `SciPy` (Virtanen et al. 2020) and `TOPCAT` (Taylor 2005). `ChatGPT`, a variant language model based on GPT-3 (Brown et al. 2020) is employed to correct grammatical errors and improve readability within the text of this work.

Appendix

Here, we show the VLASS2 images of all the Roma-BzCAT sources that our algorithm classified as 2-SIDE SEPARATED or 2-SIDE EXTENDED (i.e., likely incompatible with being blazars). There are 36 sources classified as 2-SIDE SEPARATED and 105 sources classified as 2-SIDE EXTENDED; each source was visually inspected. For every source where the visual inspection led to a classification change, we assigned a visual flag value of 1 and provided our revised visual classification in the online available resulting table. In Figures 5–10, the sources with revised classifications (VClass, refer to the result table) are marked with a star in their corresponding image.

In Figure 11, we show the 22 VLASS2 images of MOJAVE sources (see Section 5.2) classified with non-blazar-like morphology. However, 11 of them are consistent with COMPACT via visual inspection (marked with stars in Figure 11). Nevertheless, all of the remaining 11 sources with non-blazar-like morphology are likely real blazars given that all of them have reported apparent superluminal motions in the MOJAVE database (Lister et al. 2019), suggesting a jet seen at a small inclination to the line of sight. This demonstrates that even in the case of extended morphology, we cannot rule out 100% the blazar nature of the sources, and other characteristics must also be taken into account.

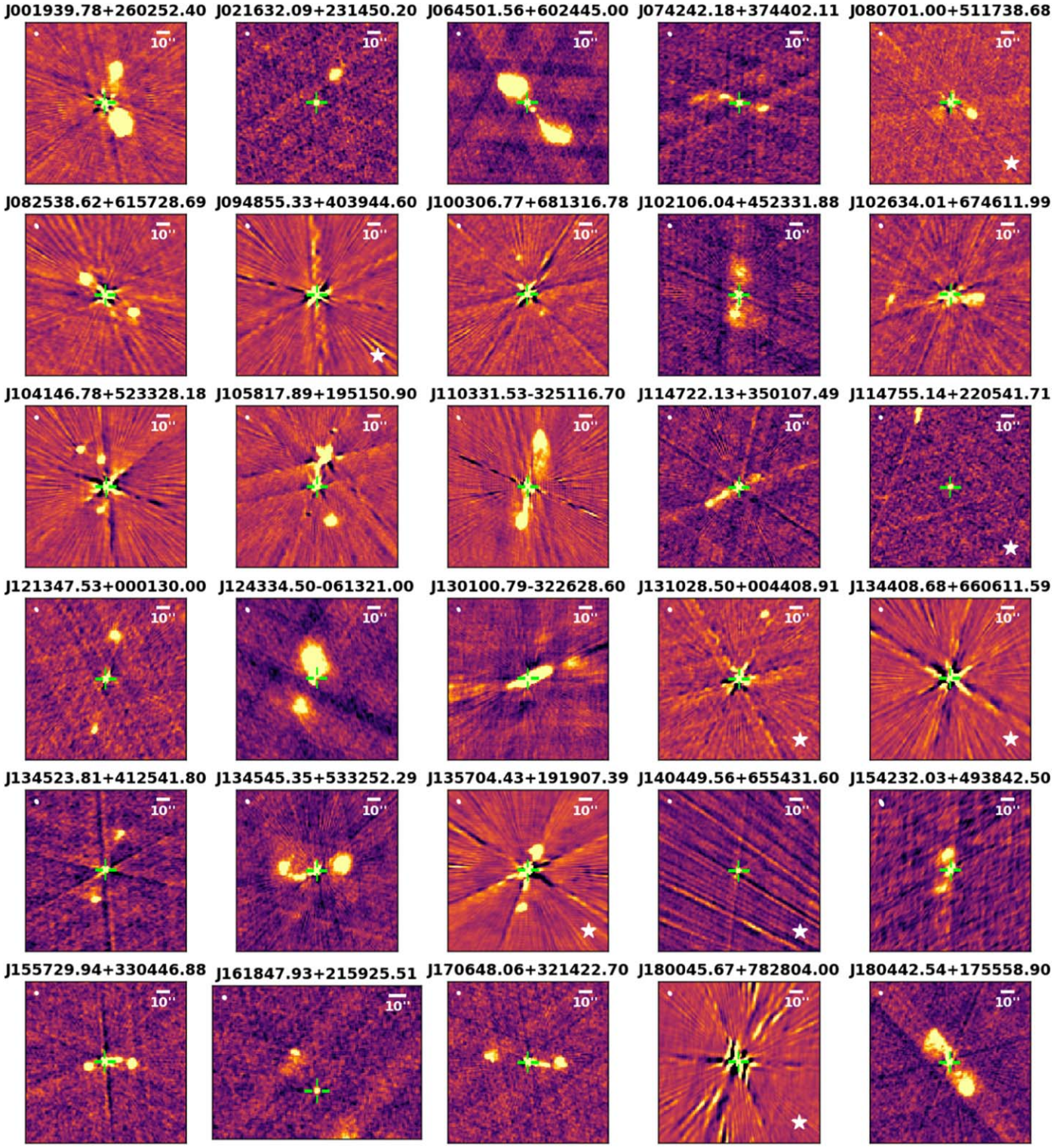

Figure 5. All 2-SIDE SEPARATED sources with their VLASS2 image in Roma-BzCAT. Each source has undergone visual inspection, and any discrepancies found during this process are indicated by a visual flag in the resulting table. For each of these sources, our revised visual classification is provided. These revised sources are marked with a white star on their image.

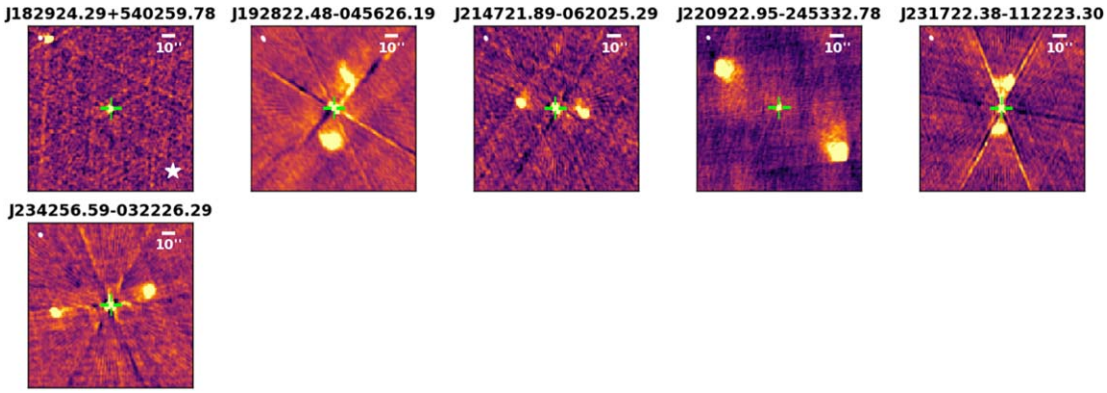

Figure 6. Continued for Figure 5.

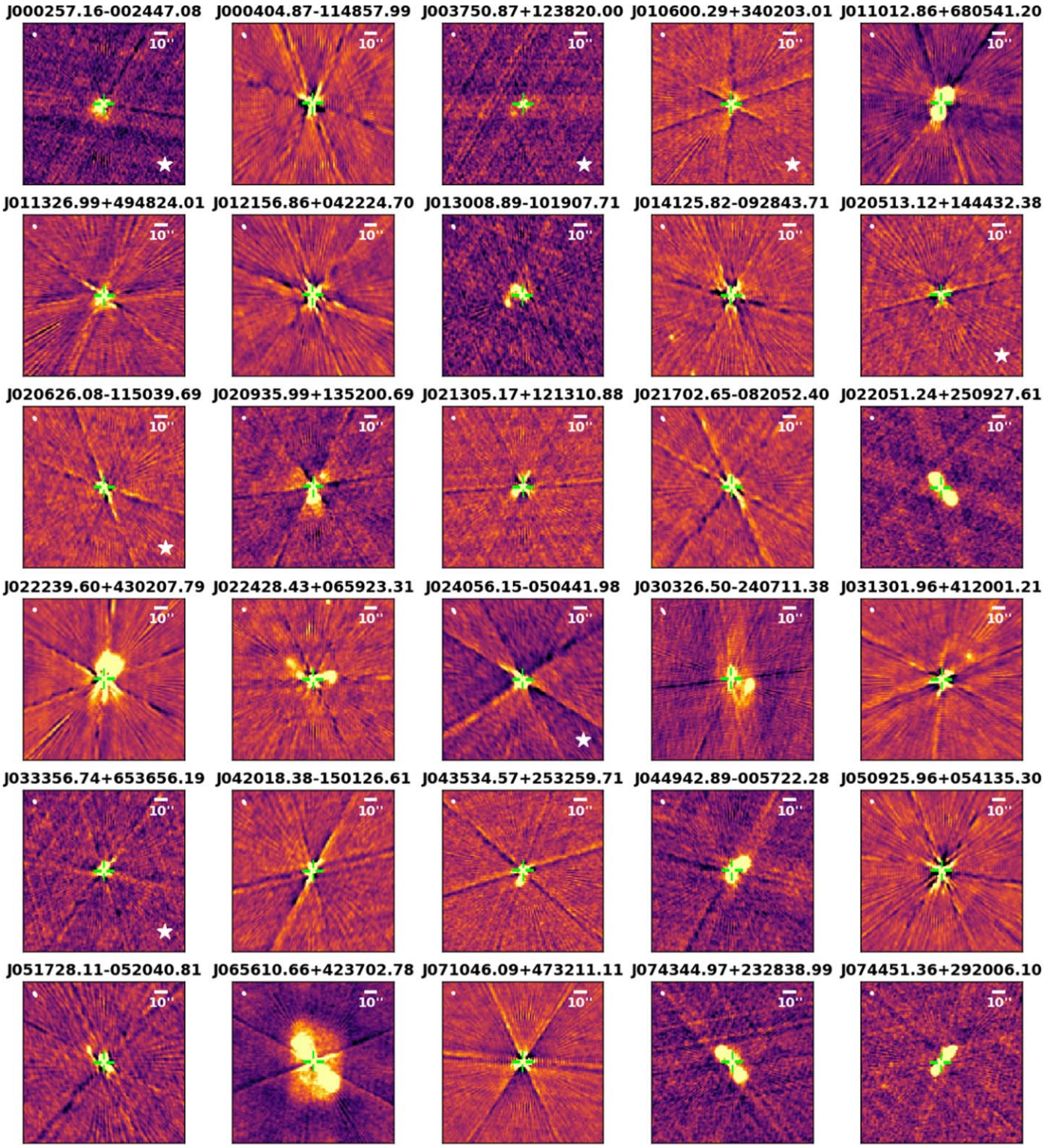

Figure 7. Same as Figure 5 but for 2-SIDE EXTENDED sources in Roma-BzCAT.

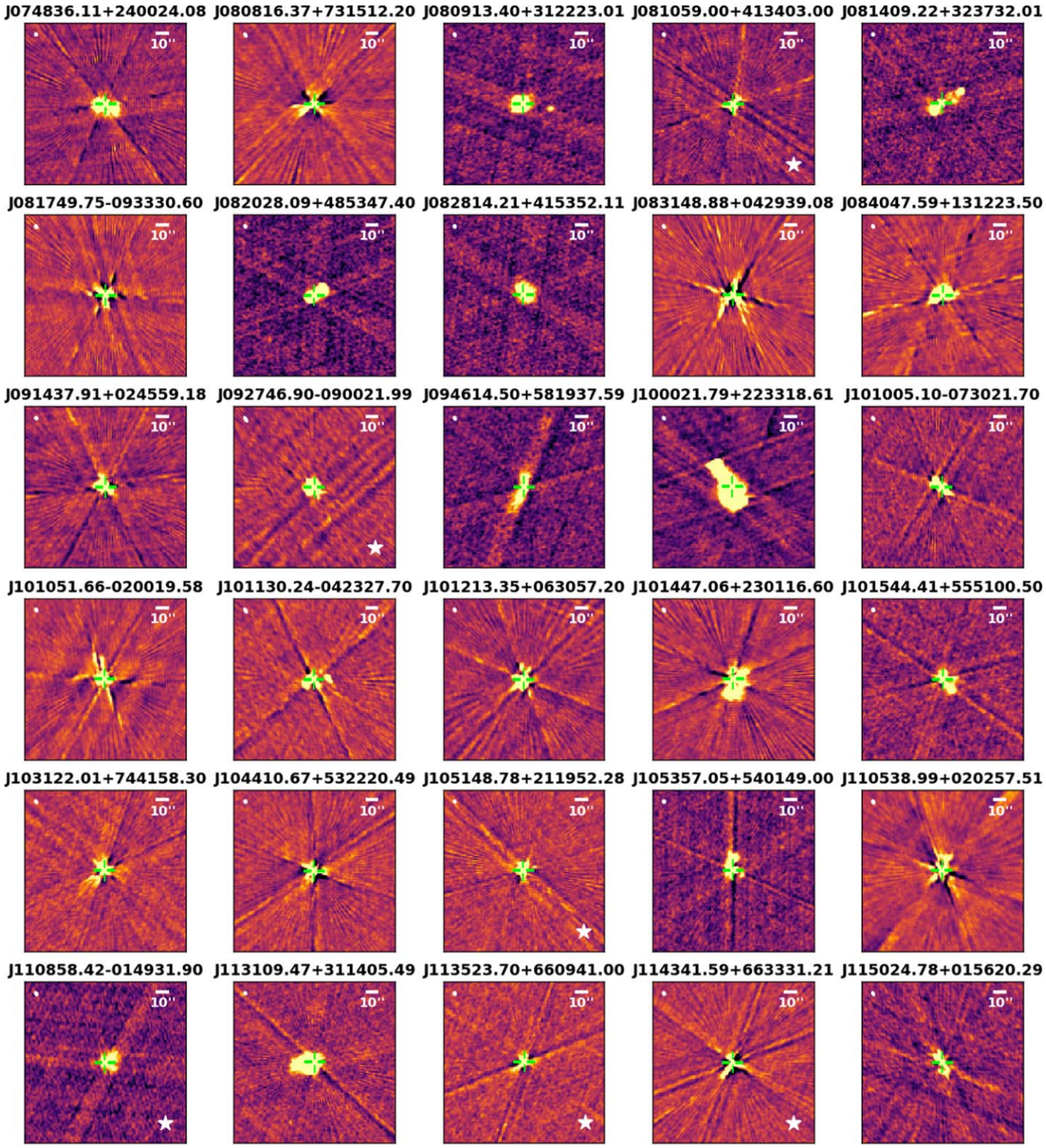

Figure 8. Continued for Figure 7.

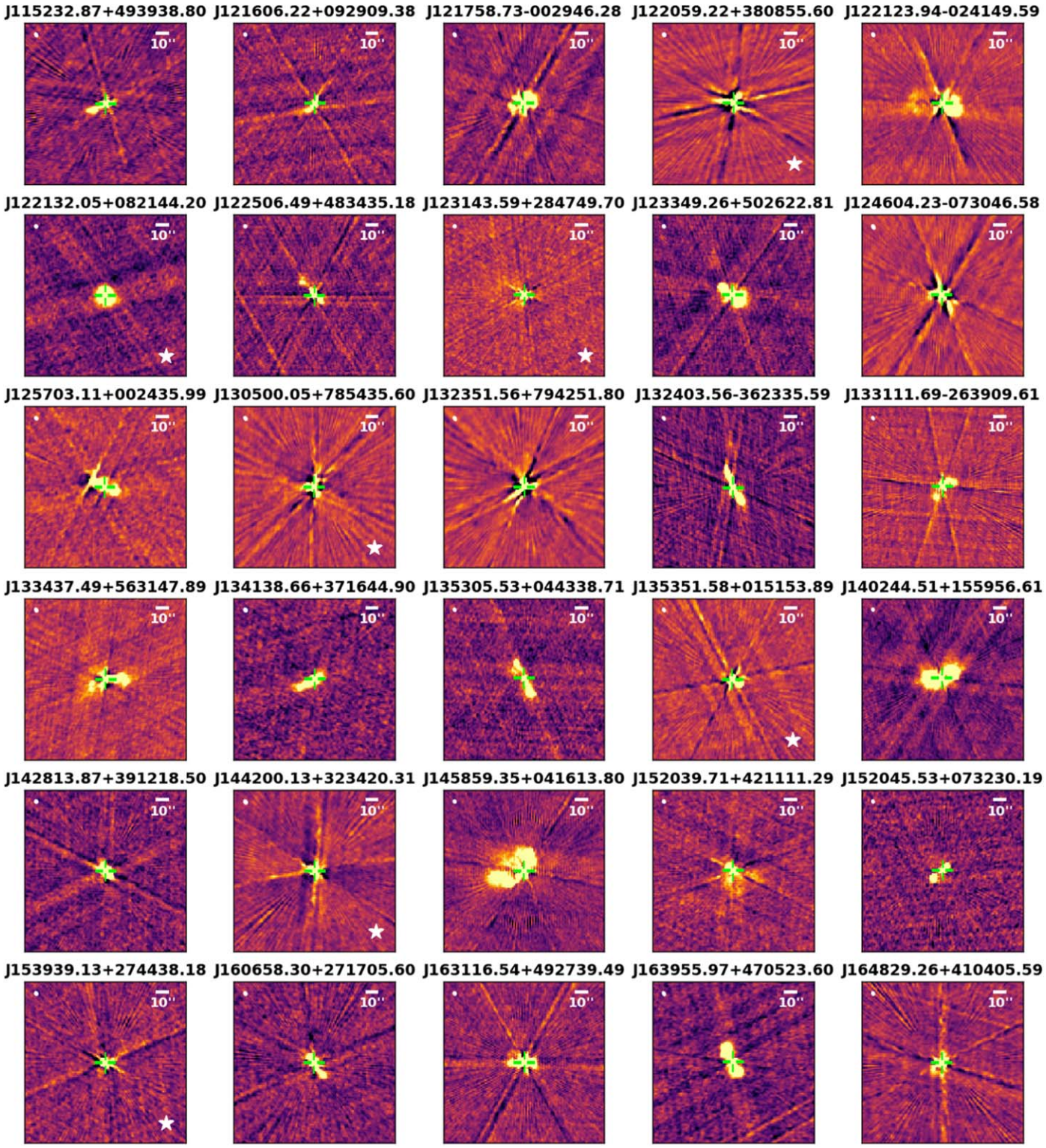

Figure 9. Continued for Figure 8.

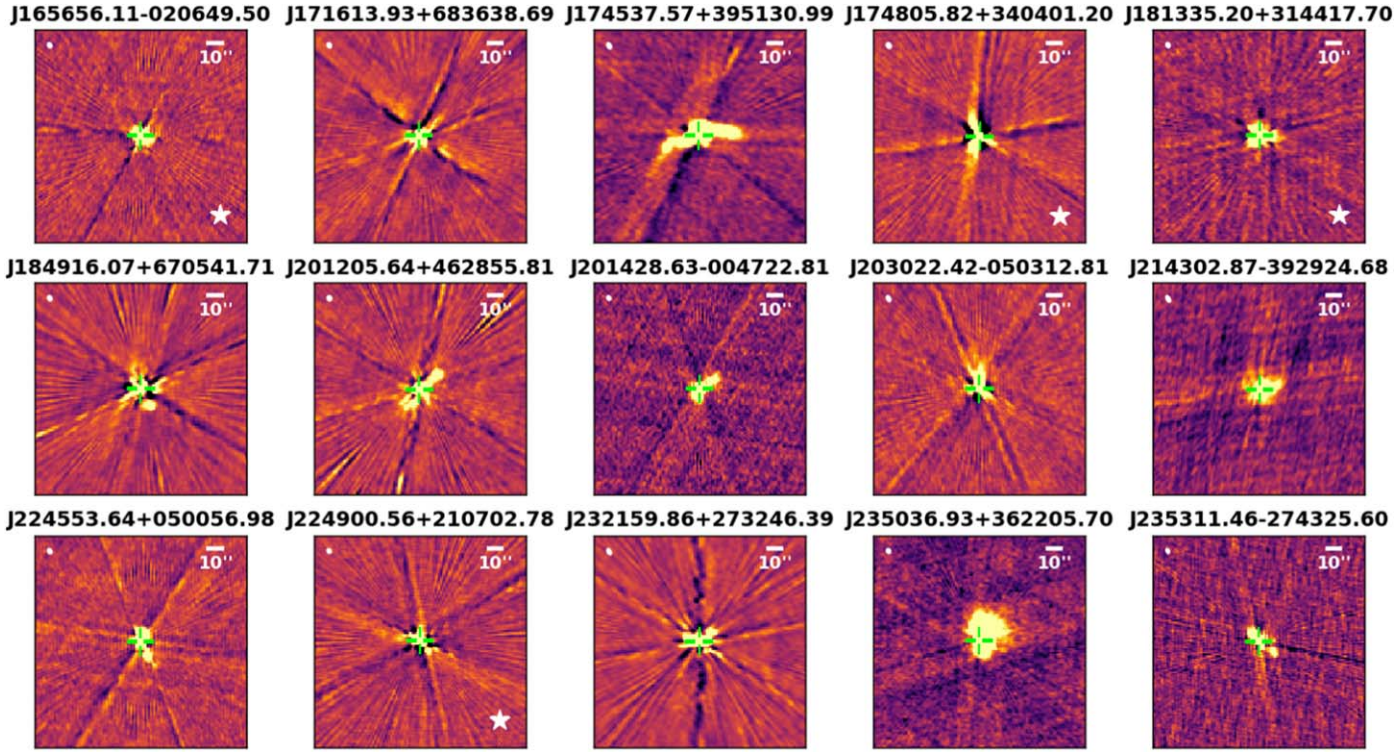

Figure 10. Continued for Figure 9.

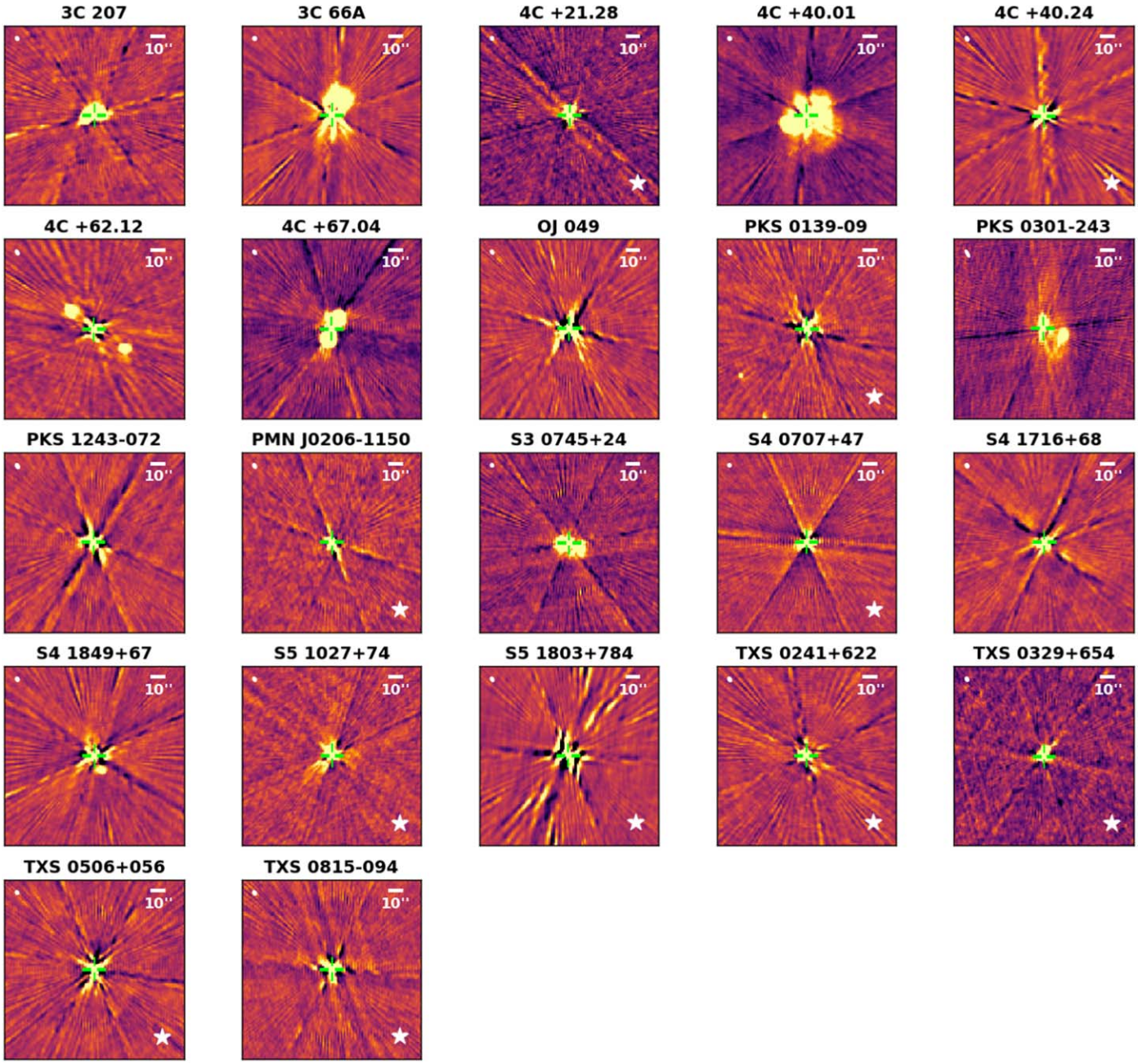

Figure 11. VLASS2 images for 22 MOJAVE blazars classified as likely non-blazars. Each source has undergone visual inspection, and any discrepancies (are COMPACT instead of NON-COMPACT) found during this process are indicated by a visual flag in the resulting table. For each of these sources, our revised visual classification is provided. These revised sources are marked with a white star on their image.

ORCID iDs

Zhang-Liang Xie (谢彰亮) https://orcid.org/0000-0002-0125-6679
Eduardo Bañados https://orcid.org/0000-0002-2931-7824
Silvia Belladitta https://orcid.org/0000-0003-4747-4484
Chiara Mazzucchelli https://orcid.org/0000-0002-5941-5214
Jan-Torge Schindler https://orcid.org/0000-0002-4544-8242
Frederick Davies https://orcid.org/0000-0003-0821-3644
Bram P. Venemans https://orcid.org/0000-0001-9024-8322

References

Abdo, A. A., Ackermann, M., Agudo, I., et al. 2010, ApJ, 716, 30
Ajello, M., Angioni, R., Axelsson, M., et al. 2020, ApJ, 892, 105
Antonucci, R. R. J., Hickson, P., Olszewski, E. W., & Miller, J. S. 1986, AJ, 92, 1
Astropy Collaboration, Price-Whelan, A. M., Lim, P. L., et al. 2022, ApJ, 935, 167
Astropy Collaboration, Price-Whelan, A. M., Sipőcz, B. M., et al. 2018, AJ, 156, 123
Astropy Collaboration, Robitaille, T. P., Tollerud, E. J., et al. 2013, A&A, 558, A33
Bauer, F. E., Condon, J. J., Thuan, T. X., & Broderick, J. J. 2000, ApJS, 129, 547

Becker, R. H., White, R. L., & Helfand, D. J. 1994, in ASP Conf. Ser. 61, Astronomical Data Analysis Software and Systems III, ed. D. R. Crabtree, R. J. Hanisch, & J. Barnes (San Francisco, CA: ASP), 165
Blandford, R., Meier, D., & Readhead, A. 2019, ARA&A, 57, 467
Blandford, R. D., & Königl, A. 1979, ApJ, 232, 34
Brown, T. B., Mann, B., Ryder, N., et al. 2020, arXiv:2005.14165
Condon, J. J., Cotton, W. D., Greisen, E. W., et al. 1998, AJ, 115, 1693
D'Abrusco, R., Álvarez Crespo, N., Massaro, F., et al. 2019, ApJS, 242, 4
D'Abrusco, R., Massaro, F., Ajello, M., et al. 2012, ApJ, 748, 68
D'Abrusco, R., Massaro, F., Paggi, A., et al. 2014, ApJS, 215, 14
de Menezes, R., Peña-Herazo, H. A., Marchesini, E. J., et al. 2019, A&A, 630, A55
Dewdney, P. E., Hall, P. J., Schilizzi, R. T., & Lazio, T. J. L. W. 2009, IEEEP, 97, 1482
European Organization For Nuclear Research & OpenAIRE 2013, CERN, Zenodo, doi:10.25495/7GXK-RD71
Flesch, E. W. 2021, arXiv:2105.12985
Ginsburg, A., Sipőcz, B. M., Brasseur, C. E., et al. 2019, AJ, 157, 98
Gordon, Y. A., Boyce, M. M., O'Dea, C. P., et al. 2021, ApJS, 255, 30
Harris, C. R., Millman, K. J., van der Walt, S. J., et al. 2020, Natur, 585, 357
Hartman, R. C., Bertsch, D. L., Bloom, S. D., et al. 1999, ApJS, 123, 79
Hunter, J. D. 2007, CSE, 9, 90
Joye, W. A., & Mandel, E. 2003, in ASP Conf. Ser. 295, Astronomical Data Analysis Software and Systems XII, ed. H. E. Payne, R. I. Jedrzejewski, & R. N. Hook (San Francisco, CA: ASP), 489
Kharb, P., Lister, M. L., & Cooper, N. J. 2010, ApJ, 710, 764
Kollgaard, R. I., Wardle, J. F. C., Roberts, D. H., & Gabuzda, D. C. 1992, AJ, 104, 1687
Lacy, M., Baum, S. A., Chandler, C. J., et al. 2020, PASP, 132, 035001
Lacy, M., Myers, S. T., Chandler, C., et al. 2022, VLASS Project Memo 13: Pilot and Quick Look Data Release v2, https://library.nrao.edu/public/memos/vla/vlass/VLASS_017.pdf
Lister, M. L., Aller, M. F., Aller, H. D., et al. 2018, ApJS, 234, 12
Lister, M. L., Homan, D. C., Hovatta, T., et al. 2019, ApJ, 874, 43
Lister, M. L., Homan, D. C., Kellermann, K. I., et al. 2021, ApJ, 923, 30
Massaro, E., Giommi, P., Leto, C., et al. 2009, A&A, 495, 691
Massaro, E., Maselli, A., Leto, C., et al. 2015, Ap&SS, 357, 75
Mauch, T., Murphy, T., Buttery, H. J., et al. 2008, yCat, VIII/81A
McKinney, W. 2010, in Proc. 9th Python in Sci Conf., ed. S. van der Walt & J. Millman, 61
Motch, C., Guillout, P., Haberl, F., et al. 1998, A&AS, 132, 341
Piranomonte, S., Perri, M., Giommi, P., Landt, H., & Padovani, P. 2007, A&A, 470, 787
Reback, J., jbrockmendel, McKinney, W., et al. 2022, pandas-dev/pandas: Pandas v1.4.2, Zenodo, doi:10.5281/zenodo.3509134
Robitaille, T., & Bressert, E., 2012 APLpy: Astronomical Plotting Library in Python, Astrophysics Source Code Library, ascl:1208.017
Sambruna, R. M., Maraschi, L., & Urry, C. M. 1996, ApJ, 463, 444
Shaw, M. S., Romani, R. W., Cotter, G., et al. 2012, ApJ, 748, 49
Stickel, M., Padovani, P., Urry, C. M., Fried, J. W., & Kuehr, H. 1991, ApJ, 374, 431
Taylor, M. B. 2005, in ASP Conf. Ser. 347, Astronomical Data Analysis Software and Systems XIV, ed. P. Shopbell, M. Britton, & R. Ebert (San Francisco, CA: ASP), 29
Tody, D. 1986, Proc. SPIE, 627, 733
Urry, C. M., & Padovani, P. 1995, PASP, 107, 803
van der Walt, S., Colbert, S. C., & Varoquaux, G. 2011, CSE, 13, 22
Virtanen, P., Gommers, R., Oliphant, T. E., et al. 2020, NatMe, 17, 261
Wagner, S. J., Witzel, A., Heidt, J., et al. 1996, AJ, 111, 2187
Wenger, M., Ochsenbein, F., Egret, D., et al. 2000, A&AS, 143, 9
Wright, E. L., Eisenhardt, P. R. M., Mainzer, A. K., et al. 2010, AJ, 140, 1868